



HAL
open science

Localization of Yb^{3+} , Er^{3+} and Co^{2+} Dopants in an Optical Glass Ceramics of MgAl_2O_4 Spinel Nano-crystals Embedded in SiO_2 Glass

Georges Boulon, Y. Guyot, G. Alombert-Goget, M. Guzik, T. Epicier, Lin Chen, L. Hu, W. Chen

► To cite this version:

Georges Boulon, Y. Guyot, G. Alombert-Goget, M. Guzik, T. Epicier, et al.. Localization of Yb^{3+} , Er^{3+} and Co^{2+} Dopants in an Optical Glass Ceramics of MgAl_2O_4 Spinel Nano-crystals Embedded in SiO_2 Glass. NATO Advanced Study Institute on Nano-Optics: Principles Enabling Basic Research and Applications, Jul 2015, Erice, Italy. pp.319-341, 10.1007/978-94-024-0850-8_16 . hal-01814374

HAL Id: hal-01814374

<https://hal.science/hal-01814374>

Submitted on 21 Jan 2022

HAL is a multi-disciplinary open access archive for the deposit and dissemination of scientific research documents, whether they are published or not. The documents may come from teaching and research institutions in France or abroad, or from public or private research centers.

L'archive ouverte pluridisciplinaire **HAL**, est destinée au dépôt et à la diffusion de documents scientifiques de niveau recherche, publiés ou non, émanant des établissements d'enseignement et de recherche français ou étrangers, des laboratoires publics ou privés.



Distributed under a Creative Commons Attribution - NonCommercial 4.0 International License

Localization of Yb³⁺, Er³⁺ and Co²⁺ Dopants in an Optical Glass Ceramics of MgAl₂O₄ Spinel Nano-crystals Embedded in SiO₂ Glass

G. Boulon, Y. Guyot, G. Alombert-Goget, M. Guzik, T. Epicier, L. Chen, L. Hu, and W. Chen

Abstract The main goal of this research is the localization of Yb³⁺ and Er³⁺ rare earth ions and Co²⁺ transition metal ion as dopants in a glass ceramics composed of MgAl₂O₄ spinel nano-crystals of 10–20 nm size embedded in SiO₂ glass. This is the first step of a compact self-Q-switched microchip laser. We conjugate, that is rather rare, both TEM-EDX and optical spectroscopy techniques. The use of TEM-EDX technique associated with both the elemental mapping of each dopant and the direct visualization of the heavier rare earth ions is unique way in luminescent materials which has led to the result that Er³⁺ and Yb³⁺ rare earth ions are preferentially located in the spinel nano-crystals. Regarding the Co²⁺ low concentration, this technique was not enough accurate and finally absorption spectroscopy technique have probed the main presence of Co²⁺ ions in the spinel nano-crystals. The use of site selective spectroscopy technique applied to Yb³⁺ structural probes allows to identify the 0-phonon broad line at 975 nm with both that of the disordered glass and that of the spinel inverted phases. A new Yb³⁺ radiationless center has been pointed out by the presence of a strong absorption line at 970 nm which has been assigned to the strongly perturbed area of the spinel nano-crystallite surface. This dopant

G. Boulon (✉) • Y. Guyot • G. Alombert-Goget
Univ Lyon, Université Claude Bernard Lyon 1, CNRS, Institut Lumière Matière, Lyon F-69622, Villeurbanne, France
e-mail: georges.boulon@univ-lyon1.fr

M. Guzik
Faculty of Chemistry, University of Wrocław, 14 F. Joliot-Curie, PL-50-383, Wrocław, Poland

T. Epicier
MATEIS, UMR 5510 CNRS, INSA of Lyon, University of Lyon, Bât. B. Pascal, 69621 Villeurbanne, France

L. Chen • L. Hu • W. Chen
High Power Laser Components R&D Center, Shanghai Institute of Optics and Fine Mechanics, Chinese Academy of Sciences, Jiading, Shanghai 201800, China

characterization worthwhile to be shown in this School by applying both TEM-EDX and optical spectroscopy techniques as a pedagogical case in the research of rare earth ions and transition metal ions localization.

16.1 Introduction

16.1.1 Evolution of Solid State Lasers from Nd³⁺/Yb³⁺-Doped Single Crystals to Nd³⁺/Yb³⁺-Doped Transparent Ceramics

Inorganic solid-state lasers based on light-pumped insulating host materials containing optically active dopants as metal transition ions (3d configuration) and rare earth ions (4f configuration) continue to occupy a prominent place among the different kinds of laser devices. Indeed, solid-state lasers are mainly used as oscillators or amplifiers in industrial, medical, military and scientific fields. The 1st laser has been demonstrated by Maiman at Hughes Lab with Cr³⁺ ions of 3d³ configuration-doped Al₂O₃ in 1960 [1], emitting the sharp line ²E → ⁴A₂ at 694.3 nm. However, this ruby laser is an inefficient three-level scheme and it was necessary to look on more efficient four-level scheme. An important breakthrough was the discovery of Nd³⁺-doped Y₃Al₅O₁₂ (YAG) garnet crystal by Geusic as four-level scheme with right parameters and its extension to Nd³⁺-doped glasses [2]. The improvement of laser efficiency of Nd³⁺-doped YAG laser crystal is a slow process: it won a factor of only two, 20 years after the first growth in 1964 [3]. During this period of time, the focus of the respective fields, namely phosphors for lighting application and solid-state lasers, has converged toward common targets, in the sense that phosphor research and development has been heavily concerned with the luminescence properties of trivalent rare earth ions, while in the research for tunable, coherent sources, the interest in laser materials has veered toward the type of band emitters traditionally investigated in phosphor research. Then scientific know-how has somehow percolated between the two fields. The information exchange from the laser field to the phosphor field has not been restricted to theoretical models but has been important in the field of materials (apatites, garnets, sesquioxides) [4]. The most important driving forces and noteworthy developments of laser materials since 1960 were the following ones [3]:

- Understanding of optical spectroscopy of luminescent ions used as laser ions,
- Laser fundamentals understandings,
- Choice and improvement of crystal growth techniques,
- Laser-diode-pumped solid state lasers as new sources,
- Polycrystalline ceramic lasers as a new generation of laser materials

16.1.2 Nd³⁺/Yb³⁺-Doped Transparent Ceramics

The recent development of ceramic laser materials is probably the most important innovation in the field of laser material fabrication technology. The large-scale laser materials are necessary for high-power laser systems. Unfortunately, the size of single-crystal is limited and, the boule cross-section shows facets giving rise to difficulties during the growth. Single crystals are generally grown from the melt and they suffer from drawbacks such as segregation of the dopant from the host, optical inhomogeneity caused by stress during crystal growth, high cost and low productivity due to high temperature processing. Transparent polycrystalline are advantageous over single crystals in many ways. The process is simple, cost effective and typically carried out at lower temperature. Most important, much higher doping concentrations in ceramics can be obtained without phase segregation as we often observe in single crystals. As a result, laser ceramics are quite attractive since 1995 and it has been possible to fabricate the large-scale laser materials by using ceramic technology applied on isotropic hosts like Y₃Al₅O₁₂ cubic garnets, (Y₂O₃) sesquioxides, MgAl₂O₄ spinels, CaF₂ fluorides [5–10]. Producers are challenging to make various large size ceramics with high optical quality under rods, disks and slabs shapes and by playing with engineer profiles and structures and also composites like un-doped and doped ceramics [11].

However, although high efficiencies have been demonstrated, one limitation can be associated with Nd³⁺ segregation at grain boundaries in transparent Nd³⁺-doped YAG ceramics for lasers [12], Ce³⁺-doped (Y,Gd)Al₃O₁₂ [13], Ce³⁺-doped YAG [14] for scintillators and also phosphors for white LED sources. Segregation was not observed in Yb³⁺-doped YAG [15, 16] or Yb³⁺-doped Y₂O₃ [16]. We have interpreted such data by the variation of segregation coefficients of rare earth ions in oxide optical ceramics like in growth of crystals from the melt and/or flux. The lower is the segregation coefficient of the luminescent ions in the melt growth, the greater amount of luminescent ions will be collected on the grain boundaries of the ceramic material [17]. It means that such segregation phenomenon can perturb kinetics of the fluorescence in transparent ceramics and then the best laser sources should be obtained with the best uniformity of Yb³⁺ and Nd³⁺ ions in optical ceramics.

16.1.3 Essays to Use Glass Ceramics

Another field of optical materials consists to develop rare earth/ transition metal ions-doped glass ceramics for laser sources or scintillators or phosphors. Until today, glass ceramics have been applied for thermal and mechanical properties. In spite of numerous experimental essays, optical properties of glass ceramics are not yet really exploited.

An original idea was proposed recently with transparent glass ceramics [18, 19] containing Yb³⁺, Er³⁺ ions in glass matrix and Co²⁺-doped MgAl₂O₄

nano-crystals of sizes of 10–20 nm, which can be used as compact self-Q-switched microchip laser. First of all, we have to show that the main conditions are fulfilled in glass ceramics for obtaining self-Q-switched microchip laser. Passively Q-switched, diode-pumped solid state lasers are currently being used as miniature or micro-lasers capable of delivering high peak output power at high repetition rates and short nanosecond (ns) temporal pulse width. These lasers are of great interest due to their potential applications in micro-machining, remote sensing, target, ranging, and microsurgery. Cr^{4+} and Co^{2+} dopants have been proposed as saturable absorbers for passive Q-switching of solid-state lasers operating in the near-infrared region. Most commonly, systems presently used are based on Nd^{3+} : YAG or Nd^{3+} : YVO_4 lasers, passively Q-switched by Cr^{4+} : YAG, where the unique well-known characteristics of Cr^{4+} garnets as saturable absorbers are applied [20–23]. Another crystal like Cr^{4+} : Mg_2SiO_4 was also proposed as saturable absorber [24]. The most important application of the oxide crystals doped with tetrahedrally coordinated Co^{2+} ions is passive Q-switching of solid-state lasers operating in the near-infrared region. A number of crystals such as YAG, $\text{LaMgAl}_{11}\text{O}_{19}$ (LMA), ZnSe was doped with Co^{2+} ions [25, 26]. As an example, passively Q-switched 1.34 μm Nd^{3+} : $\text{Y}_x\text{Gd}_{1-x}\text{VO}_4$ laser with Co^{2+} : $\text{LaMgAl}_{11}\text{O}_{19}$ saturable absorber was demonstrated [27].

Indeed, glasses containing nano-crystals embedded in a glass matrix can enhance existing or offer completely new properties compared to those of the precursor glass. These transparent glass ceramics possess the spectral requirements of both eye safe lasers by Er^{3+} ${}^4\text{I}_{13/2} \rightarrow {}^4\text{I}_{15/2}$ emission in glass matrix between 1.5 and 1.6 μm under Yb^{3+} pumping and saturable absorbers by ${}^4\text{A}_2(\text{F}) \rightarrow {}^4\text{T}_1(\text{F})$ transition of Co^{2+} -doped MgAl_2O_4 nano-crystals so that, together, might be developed as self-Q-switched microchip laser. Obviously, the morphology of this new class of optical materials requires to solve the specific characterisations of the location of dopants in the two glassy and nano-spinel phases in order to check the feasibility of this system.

Consequently, the main goal of this lecture presented at the School is to conjugate TEM-EDX and optical spectroscopy tools to localize Yb^{3+} , Er^{3+} and Co^{2+} dopants in a glass ceramics composed of MgAl_2O_4 spinel nano-crystals of 10–20 nm size embedded in the SiO_2 glass [28].

16.2 Experimental Techniques

16.2.1 Sample Preparation

Glass with a composition (in wt. %) of 1.8 Yb_2O_3 -1.7 Er_2O_3 -11 MgO -31.5 Al_2O_3 -47 SiO_2 -4.5 TiO_2 -2.5 ZrO_2 -0.03 CoO (C_YE glass) was prepared, where TiO_2 and ZrO_2 were used as mixed nucleating agents [19]. Concentrations of Co^{2+} , Yb^{3+} and Er^{3+} ions are $5.77 \times 10^{18} \text{ cm}^{-3}$, $1.5 \times 10^{20} \text{ cm}^{-3}$, and $1.46 \times 10^{20} \text{ cm}^{-3}$, respectively. For comparison, CoO -un-doped glass (Y_E glass) with the same

composition was also prepared. For two glasses, homogeneous mixtures (300 g) of analytical reagent grade raw materials, obtained by ball milling, were melted in a corundum crucible in a laboratory electric furnace at 1580 °C for 4 h in air atmosphere with stirring. According to differential scanning calorimetry (DSC) analysis, CYE and YE glass samples were heat treated at 760 °C for 12 h, and then at 930 °C for 4 h. As a result, transparent CYE GC and YE GC were synthesized. The purity of Yb₂O₃ and Er₂O₃ is 4 N, while other reagents are analytical grade.

For comparative absorption analysis of samples containing different concentrations of Yb³⁺ and one Er³⁺ concentration we used the compositions (in wt.%) of 2Yb₂Er, 4Yb₂Er, and 6Yb₂Er, it means xYb₂O₃-1.1Er₂O₃-(3.3-x)La₂O₃-11MgO-30.6Al₂O₃-47SiO₂-4.5TiO₂-2.5ZrO₂-0.03CoO (x = 1.1, 2.2, 3.3), respectively.

16.2.2 Experimental Section

16.2.2.1 TEM-EDX Experiments

Experiments were conducted on the Cs-corrected TITAN Environmental Transmission Electron Microscope (ETEM) from FEI installed at CLYM (Centre Lyonnais de Microscopie, University of Lyon, www.clym.fr) and operated at 300 kV. Thin foils were prepared by ion bombardment (PIPS system from GATAN). According to this preparation method, some Ar⁺ has been detected during EDX analysis with a SDD analyzer from Oxford Instruments (classical implantation of Ar⁺ ions in glassy phases). Cu is also detected as spurious elements due to the sample environment in the microscope. During TEM work, irradiation effects were encountered due to the high electron flux at 300 kV. However, all reported observations were obtained in reasonably short times and prior to any significant degradation (e.g. drift, deformation or detectable structural chemical variation), unless otherwise specified. Especially, chemical analysis in EDX were limited to reduced doses and short acquisition times, thus limited the signal-to-noise ratio and the sensitivity of the measurements to detect the very small concentrations of Yb³⁺, Er³⁺, Co²⁺ dopants. Under these conditions, both the detection limit and the accuracy of the present results are estimated to be about 0.2 at.% for all species of special interest, i.e. the Yb³⁺, Er³⁺ and Co²⁺ doping ions. Nano-probe analysis and EDX elementary maps in the Scanning TEM (STEM) mode was performed using a probe of about 2–4 nm (Full-Width at Half-Maximum). Micrographs were acquired in both Cs-corrected High Resolution, and High Angle, Annular dark Field (HAADF) STEM modes.

16.2.2.2 Absorption Spectroscopy

Absorption spectra of glass and glass ceramic samples were measured both, at SIOM (Shanghai), at 293 K, using a Perkin Elmer UV/Visible/NIR Lambda 900 spectrophotometer in 300–2000 nm, and at the Faculty of Chemistry of the

University of Wroclaw (Poland), at 293 K and 4 K, in the same spectral range with a Cary-Varian 5000 Scan spectrometer equipped with an Oxford CF 1204 helium flow cryostat. In addition, a special thin layer technique was used to detect the $4f \rightarrow 4f$ transitions of well-grounded nano-powder of Yb^{3+} -doped spinel samples. These homogenous samples were compressed in the form of pellets under 20 MPa pressure. Transparent samples prepared in this way were used for the absorption measurements only of the Yb^{3+} -doped spinel nano-powder.

16.3 Results and Discussion

16.3.1 Morphology of Samples Observed by TEM Measurements

A typical STEM-HAADF image is presented in Fig. 16.1a where spinel nanoparticles appear with a brighter contrast with respect to the vitreous matrix. Their size ranges typically between 4 to 20 nm with an average at around 10 nm. Lattice imaging clearly indicates the crystalline nature of the spinel phase as shown in Fig. 16.2. Crystallographic indexing was performed either in the conventional diffraction mode or by using Fourier transforms, or diffractograms, of the HREM images as reported as an insert in Fig. 16.2: all acquired data are fully consistent with the usual spinel, Fd-3 m structure of MgAl_2O_4 with $a = 0.808$ nm. A confirmation of this finding is presented in Fig. 16.3 where a spinel crystallite is observed at High Resolution in the [001] viewing direction.

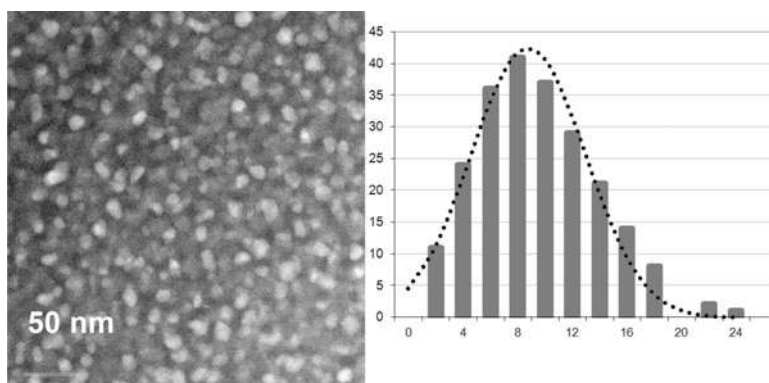


Fig. 16.1 (a) Typical STEM-HAADF image showing the distribution of spinel nanocrystallites embedded in the silicate glassy phase (spinel nanoparticles appear with a brighter contrast with respect to the vitreous matrix). (b) Size histogram of micrograph shown in a); a mean equivalent (Ferret's) diameter of 10 ± 0.3 nm can be deduced from a Gaussian fit (*dotted curve*)

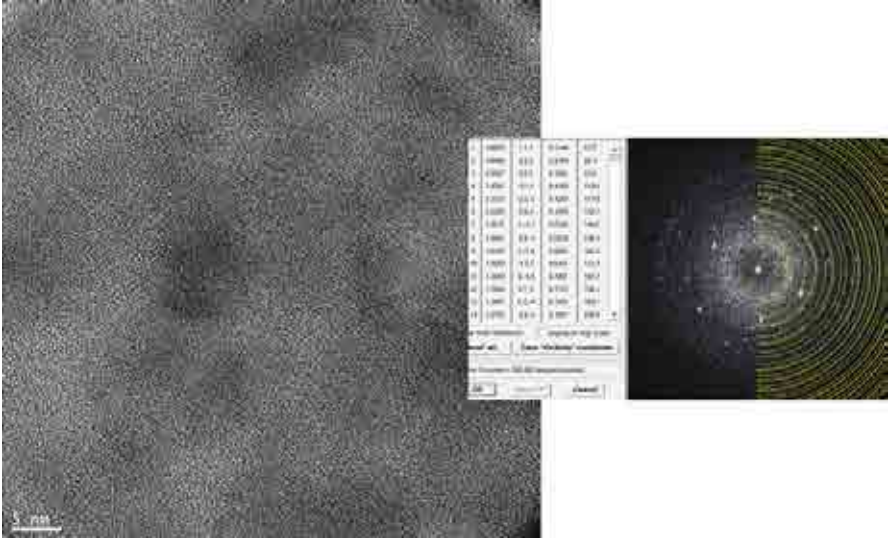


Fig. 16.2 Low magnification HRTEM micrograph and associated Fourier transform (diffractogram): diffraction rings produced by the nano-crystallite lattice planes can be consistently indexed as the prominent reflections from the expected spinel phase MgAl_2O_4 (Fd-3 m with $a = 0.808 \text{ nm}$)

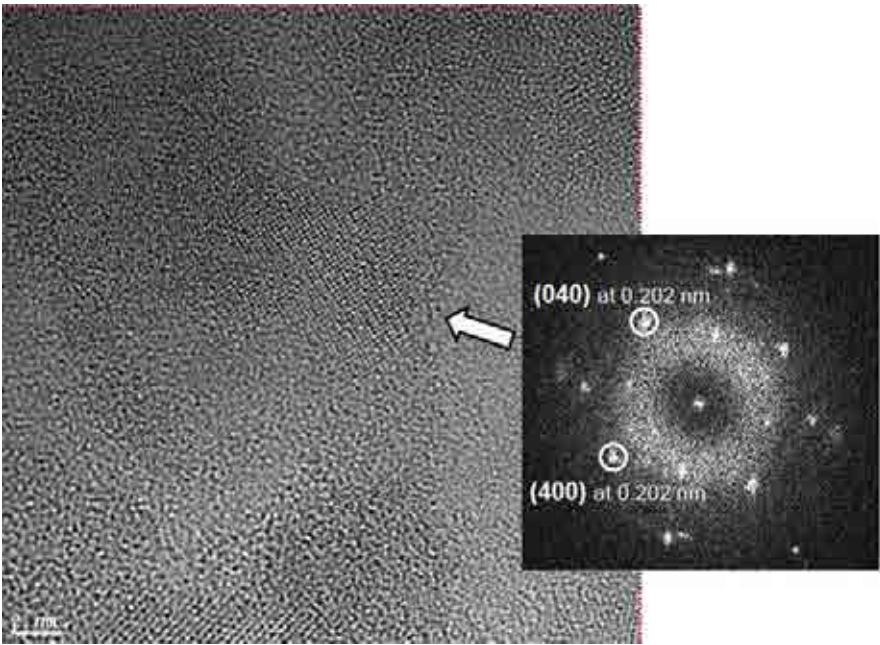


Fig. 16.3 Typical HRTEM image and indexed diffractogram of a nano-crystallite (*arrowed*). Lattice distances correspond to the usual spinel structure within a 2% accuracy

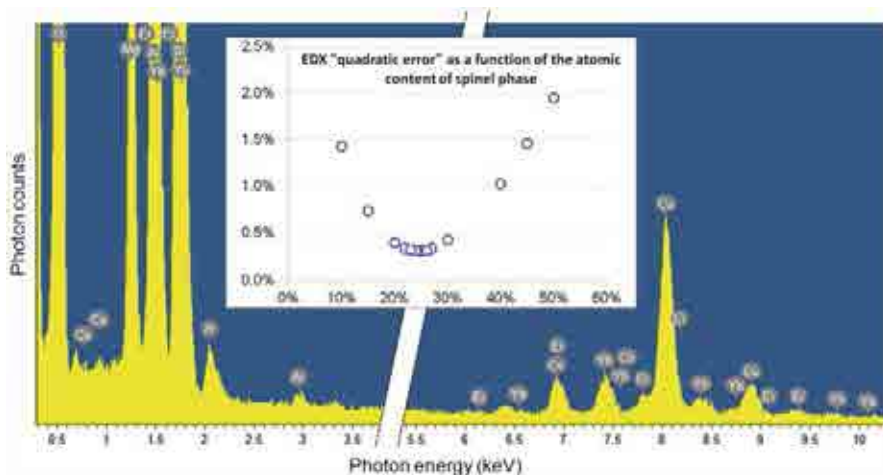


Fig. 16.4 Quantification of the spinel vs. vitreous matrix ratio: the chemical composition deduced from an EDX analysis of a large area is fitted by the following linear combination (LC): $x \text{MgAl}_2\text{O}_4 + (1-x) \text{SiO}_2$ where x represents the atomic fraction of the spinel phase; the quadratic error define d as: $R^2 = ([\text{O}]_{\text{LC}} - [\text{O}]_{\text{EDX}})^2 + ([\text{Mg}]_{\text{LC}} - [\text{Mg}]_{\text{EDX}})^2 + ([\text{Al}]_{\text{LC}} - [\text{Al}]_{\text{EDX}})^2 + ([\text{Si}]_{\text{LC}} - [\text{Si}]_{\text{EDX}})^2$ presents a minimum for about 25 at% of spinel phase. The detection of Zr and Ti (no shown) arises from the presence of ZrO_2 and TiO_2 constituents added in the starting compound to make the glass ceramics (they were not considered in the quantification)

This is important to evaluate the ratio between the MgAl_2O_4 nano-spinel crystallites and the SiO_2 glassy phase. To do so, EDX results obtained on large areas of about $1 \mu\text{m}^2$ were fitted by a linear combination of the expected chemical formulae of both phases: $x \text{MgAl}_2\text{O}_4 + (1-x) \text{SiO}_2$, where x represents the atomic fraction of the spinel phase. According to the usual consideration of absorption effects, linked to the sample thickness (estimated here to about 50 nm, with little incidence on the final spinel fraction in the interval 0–100 nm), the elemental contents for the major constituents O, Mg, Al, Si were deduced from the experimental and the spinel atomic fraction x was refined from a simple mean-least square fitting procedure (see Fig. 16.4): using this approach, an optimum value of $x = 25 \%$ was found.

16.3.2 *Distribution of Yb^{3+} , Er^{3+} , Co^{2+} Dopants as Revealed by Nano-probe EDX*

One main challenge of the present structural characterization is to know not only the distribution of Yb^{3+} , Er^{3+} , Co^{2+} dopants in both glassy and crystalline phases, but also at the interface between the nano-spinel crystals and the glass. The greatest difficulty when applying TEM-EDX technique is to find out adequate thin regions where no or very little overlap occurs between nano-crystals, due to

high concentration of nano-crystals. EDX nanoprobe analysis was performed using the classical line scan procedure as employed previously to study the distribution of Yb^{3+} ions in grains and grain boundaries in Ce^{3+} -doped YAG ceramic bulky samples [13, 14], Yb^{3+} -doped YAG and Yb^{3+} -doped Y_2O_3 ceramic bulky samples [15, 16] and Yb^{3+} -doped YAG nano-ceramics [29].

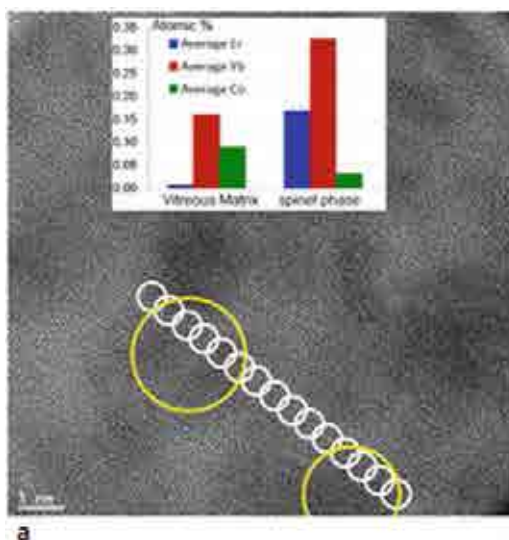
16.3.2.1 TEM-EDX Well Adapted for Rare Earth Dopants But Not for Cobalt Dopant

A typical analysis is shown in Fig. 16.5. As can be seen from the HREM micrograph, we have chosen here a region where two spinel crystallites are surrounded by the glassy matrix, where no lattice fringes were resolved. 15 measurements were performed using a probe of about 3 nm, as indicated by the circle marks. The diagram in Fig. 16.5a, b shows the evolution of the Yb^{3+} , Er^{3+} and Co^{2+} contents: enrichment in rare earth ions is clearly evidenced in the spinel phase whereas slight enrichment of the vitreous matrix is suggested by these data. We have to mention that the very low content measured for Co^{2+} and the strong overlapping between Co^{2+} and Er^{3+} high intensity lines as seen in Fig. 16.6, do not permit any definitive conclusion about any possible Co^{2+} distribution heterogeneity.

16.3.2.2 Interest of EDX Elementary Maps

To give a better global view of the dopant distribution, EDX elementary maps were recorded. Because of irradiation effects severely limiting the acceptable dose on the

Fig. 16.5a Typical HRTEM: Energy-Dispersive X-ray spectroscopy line scan applied to the same Yb-Er-Co-doped glass ceramic sample analyzed in Fig. 16.2b (probe size is about 3 nm). The two yellow zones are analyzed as spinel 1 and spinel 2 in Fig. 16.5b



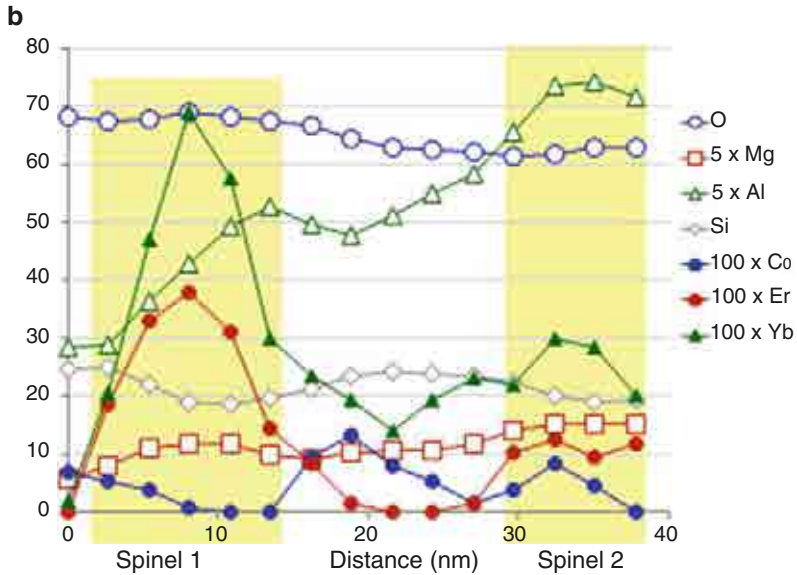


Fig. 16.5b Single spot analysis of the line scan of Fig. 16.5a. Two nano-crystallites so-called spinel 1 and spinel 2 are emphasized by the maxima of Mg, Al, Yb, Er, Co elements. Amplified intensities are applied (X 5) for Mg and Al constituents of $MgAl_2O_4$ nano-crystals and (X 100) for Yb, Er, Co dopants

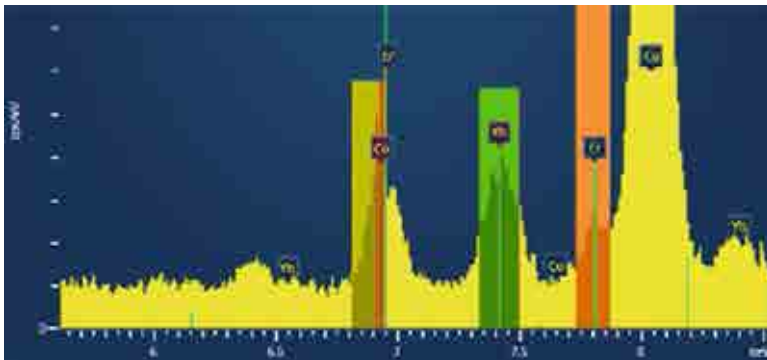


Fig. 16.6 Illustration of the major difficulty met with Co, which do not exhibit 'isolated' X-ray lines. The overlap between Er and Co high intensity lines is clearly seen

sample, it could not be possible to acquire maps with sufficient X-rays counting for an accurate quantitative treatment. However, semi-quantitative analysis gave reasonable results in agreement with previous nano-probe data, as shown by the representative montage reported in Fig. 16.7.

The elemental maps for the major species (Al, Si) allow easily the $MgAl_2O_4$ spinel and the SiO_2 vitreous matrix to be separated; as already shown in Fig. 16.1,

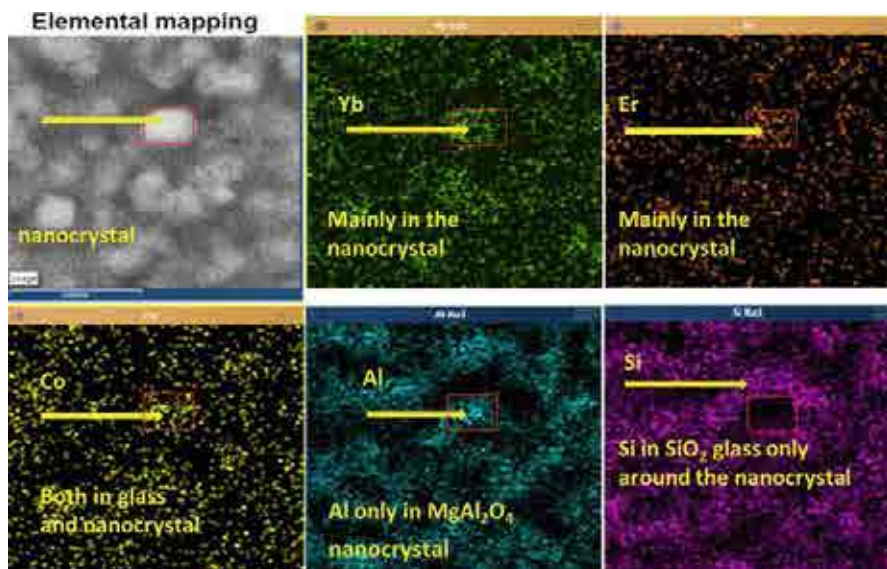


Fig. 16.7 Typical semi-quantitative elemental mapping of the Yb^{3+} , Er^{3+} , Co^{2+} dopants and the Al^{3+} component of the nano-crystalline phase and Si^{4+} component of the vitreous phase. The scale of 500 nm for all diagrams is shown in the *left* side of the first image showing the position of the analyzed nano-crystal

darker areas in STEM-HAADF images corresponds to the vitreous SiO_2 -based phase. These maps are treated in a quantitative way by the Aztec commercial software provided by the manufacturer of the EDX system, which means that overlap effects between X-ray lines is in principle correctly taken into account. According to this, the Yb^{3+} and Er^{3+} maps clearly confirm the greatest concentrations of Yb^{3+} , Er^{3+} dopants inside the nano-crystalline phase and much lower traces inside the SiO_2 glassy phase. Again, the Co^{2+} content appears too low in average and its strongest line overlaps too strongly with Er^{3+} line one, to rightly conclude about Co^{2+} ion distribution.

16.3.2.3 Direct Observation of Heavy Yb^{3+} and Er^{3+} Rare Earth Individual Ions

Another original worthwhile observation should be mentioned here concerning the HRTEM imaging of individual dopants. According to (i) the resolution permitted by the spherical aberration corrector, (ii) the large ‘weight’ (atomic number) difference between rare earth ions (Er^{3+} , Yb^{3+}) compared to the spinel and glassy phase elements (O^{2-} , Al^{3+} , Mg^{2+} , Si^{4+}), it can be postulated that in the thinnest regions, an ‘absorption-type’ contrast could allow the direct visualization of heavier rare earth individual ions. In convenient so-called ‘Scherzer images’, atoms are expected

Fig. 16.8a Typical Yb^{3+} and Er^{3+} ions as observed by *black points* in spinel nanoparticle as seen with a set of lattice planes resolved and also in glass.

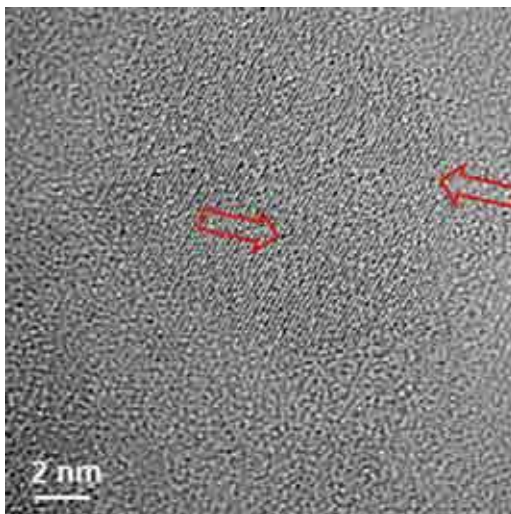
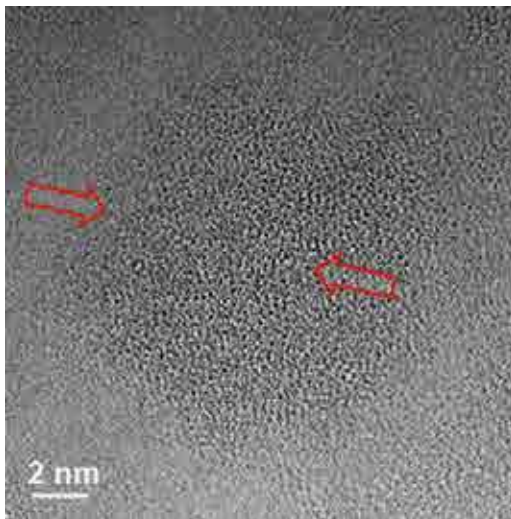


Fig. 16.8b Typical Yb^{3+} and Er^{3+} ions as observed by *black points* in spinel nanoparticle as seen “of axis”



to appear as dark dots on a brighter background. Figures 16.8a and 16.8b can be examples of such an experimental evidence in which this is even possible to distinguish rare earth pairs. We note that rare earth ions are mainly detected in the spinel nano-crystal phase. An interesting data is the possibility to observe Yb^{3+} - Yb^{3+} pairs also detected by cooperative luminescence in many Yb^{3+} -doped crystal or ceramic materials or here in glass ceramics which should be only doped by Yb^{3+} .

As a general conclusion of this TEM-EDX analysis, elemental maps of Fig. 16.7 (and, to some extent, HREM imaging in Fig. 16.8) confirm the results obtained from simple line scans in Figs. 16.5 and 16.6, less representative from the point of view of spatial distribution but more representative from a quantitative point of view: Er^{3+}

and Yb^{3+} ions are preferentially located in the spinel nano-crystallites. This is “a priori” the same conclusion for Co^{2+} ions but again the low concentration of this ion and the overlapping with Er^{3+} line cannot permit any unambiguous location so that we need some useful help from the spectroscopic data as related in the next section.

In parallel, we did not measure any significant gradient or segregation phenomenon, especially for Yb^{3+} and Er^{3+} ions, in the area of the interface between the spinel nano-crystals and the vitreous phase, although the induced damages from irradiation did not make possible to perform long acquisitions which would have been needed to gain the desirable sensitivity. This segregation was never seen for Yb^{3+} heavy ions in garnets and sesquioxides, but was encountered for example in the grain boundaries of the YAG ceramics doped with the first Nd^{3+} and Ce^{3+} rare earth ions [14–17]. As we will discuss it later, Yb^{3+} spectroscopic characterizations give some information on Yb^{3+} location on the disturbed surface of the nano-crystals.

16.3.3 Spectroscopic Properties of the Glass and the Glass Ceramic Samples

16.3.3.1 Absorption Spectra of Co^{2+} , Yb^{3+} and Er^{3+} Ions in the Visible and the IR Spectral Ranges

The absorption spectra of a glass ceramic sample shown in Fig. 16.9a, b are composed of both sharp lines from Er^{3+} and Yb^{3+} rare earth ions and broader bands from Co^{2+} transition metal ions.

We can easily see the usual Er^{3+} ion transitions from the $^4\text{I}_{15/2}$ ground state: $^4\text{I}_{15/2} \rightarrow ^2\text{H}_{9/2}$ (~407 nm), $^4\text{I}_{15/2} \rightarrow ^4\text{F}_{3/2}$ (442 nm), $^4\text{I}_{15/2} \rightarrow 4\text{F}_{5/2}$ (451 nm), $^4\text{I}_{15/2} \rightarrow ^4\text{F}_{7/2}$ (~488 nm), $^4\text{I}_{15/2} \rightarrow ^2\text{H}_{11/2}$ (~521 nm), $^4\text{I}_{15/2} \rightarrow ^4\text{S}_{3/2}$ (~543 nm), $^4\text{I}_{15/2} \rightarrow ^4\text{F}_{9/2}$ (~653 nm), $^4\text{I}_{15/2} \rightarrow ^4\text{I}_{9/2}$ (~797 nm) (not presented here), $^4\text{I}_{15/2} \rightarrow ^4\text{I}_{11/2}$ is hidden by $^2\text{F}_{7/2} \rightarrow ^2\text{F}_{5/2}$ of Yb^{3+} ions which have much higher absorption strength (965–985 nm) and $^4\text{I}_{15/2} \rightarrow ^4\text{I}_{13/2}$ (1510–1540 nm), respectively. In order to better understand the assignments of the electronic transitions we remind the energy level diagram of Er^{3+} and Yb^{3+} ions in Fig. 16.10.

As for Co^{2+} ions, we detect the presence within two spectral ranges by the transition of both $^4\text{T}_{1g} \rightarrow ^4\text{T}_{1g}$ (^4P) (expected approximately O_h symmetry of glass) and $^2\text{A}_1\text{I}^2\text{T}_2(^2\text{G}) + ^4\text{T}_1(^4\text{P}) + ^2\text{E}^2\text{T}_1(^2\text{G})$ (T_d Co^{2+}) (expected T_d symmetry of Mg^{2+} site in MgAl_2O_4 spinel nano-crystals) between 500 and 680 nm and, in the near IR, between 1100 and 1700 nm, mainly by the $^4\text{A}_2 \rightarrow ^4\text{T}_1(^4\text{F})$ (T_d Co^{2+}) of the T_d symmetry in nano-spinels. This superposition of the two types of transitions justify the potentiality of this glass ceramic composition as saturable absorbers since the Co^{2+} broad absorption overlaps widely the expected laser emission from the Er^{3+} emission near 1550 nm. It has been already shown that this sample possesses excellent transparency up to nearly 87 % at the near-infrared band [19].

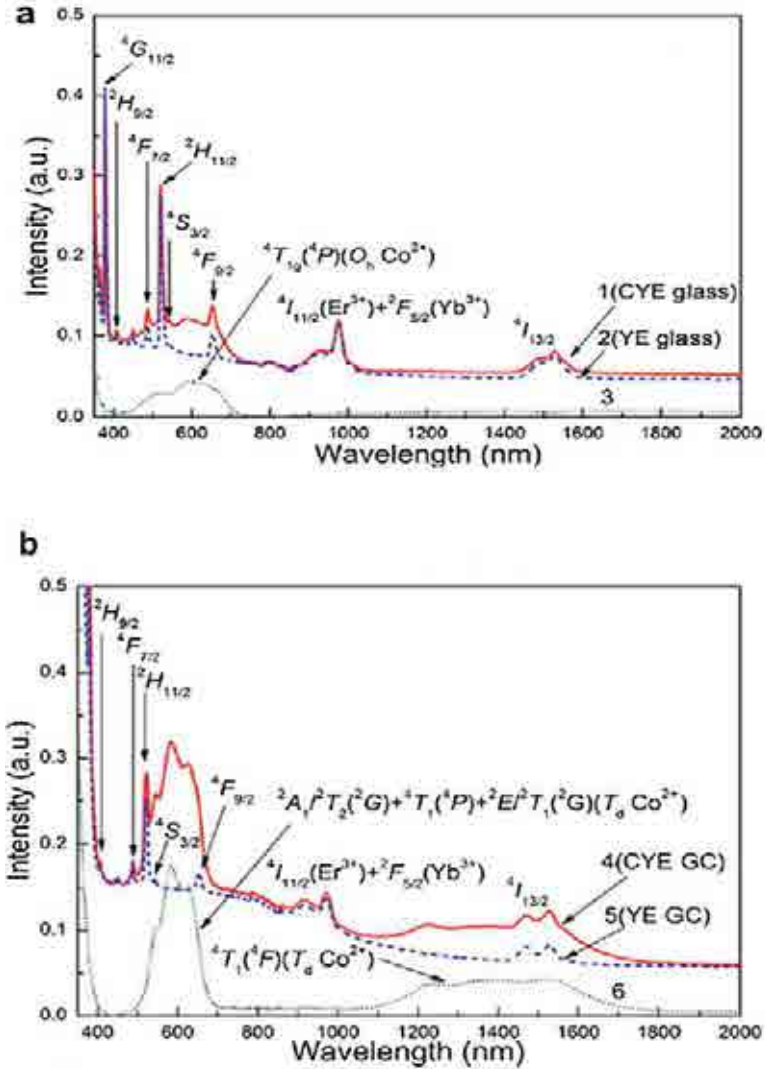


Fig. 16.9 (a) Comparison of the absorption of Co-Yb-Er-doped silicate glass (CYE glass) sample with respect of Yb-Er-doped silicate glass (YE glass) at RT. Co^{2+} ion absorption in glass has been deduced [19]. (b) Comparison of the absorption of Co-Yb-Er-doped glass ceramic (CYE-GC) sample with respect of Yb-Er-doped silicate glass (YE glass) at RT. Co^{2+} ion absorption mainly into Mg^{2+} sites of MgAl_2O_4 nano-crystals glass ceramics has been deduced [19]

16.3.3.2 Discussion on the Location of Co^{2+} Ions in Glass Ceramics

In the previous paper [19], the question on the location of Yb^{3+} and Er^{3+} rare earth ions as dopants in the glass ceramics from spectroscopic data has not been

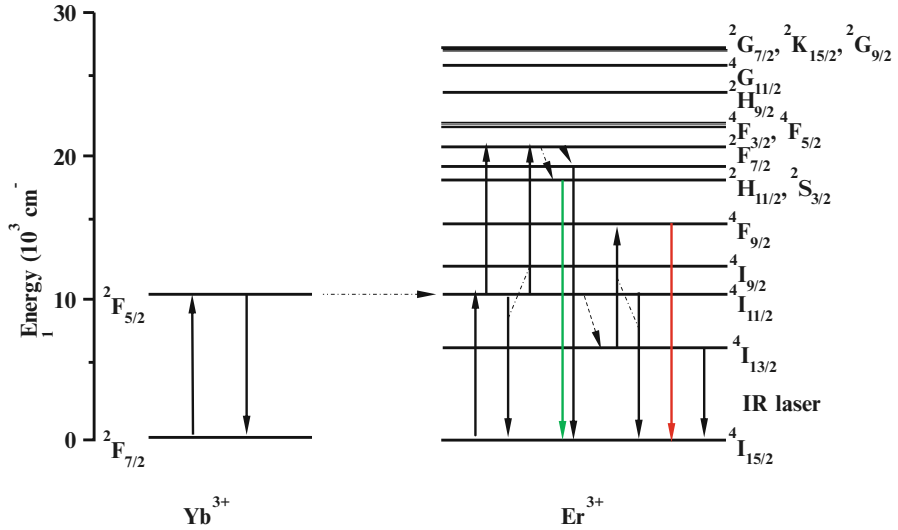


Fig. 16.10 Energy level diagram of Yb^{3+} and Er^{3+} ions in materials. The main down and up transitions are mentioned

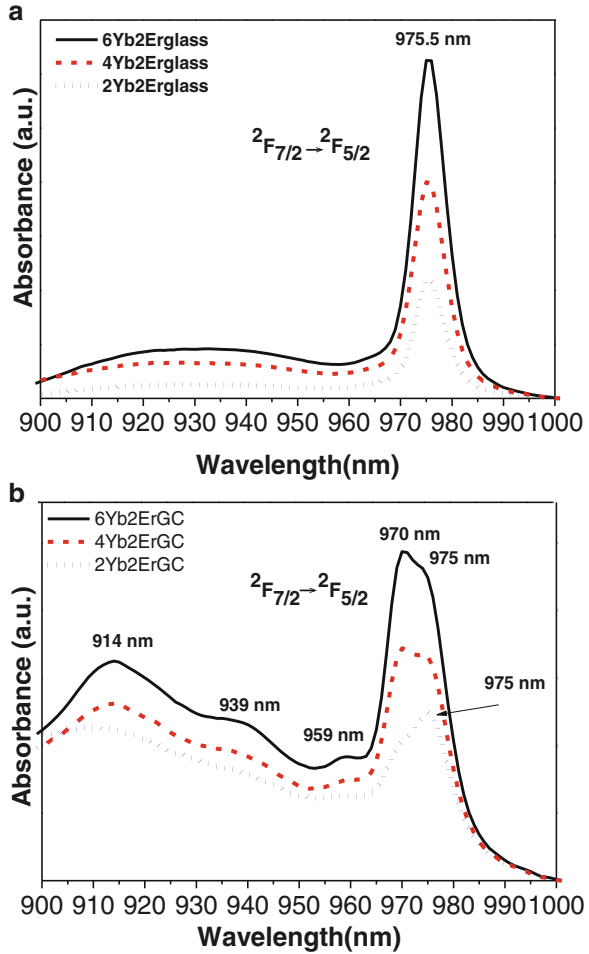
unambiguously solved, the assignment of Co^{2+} ions was only clearly established between glass and MgAl_2O_4 spinel nano-crystals of the glass ceramics. Let's remind that Co^{2+} ions optical transitions belong to transition metal ions with high oscillator strength ($f \sim 10^{-2}$) and high absorption cross-section in crystals much easier to detect than rare earth ions which are characterized by much smaller $f \sim 10^{-6}$ one. Consequently, Co^{2+} ions can be seen at low concentration on absorption spectra as it has been described here and can allow to give complementary results which were not obtained by TEM-EDX due to the overlapping of Co^{2+} and Er^{3+} X-Ray lines.

We show in Fig. 16.9a the weak Co^{2+} near infrared absorption in glass as mentioned by the spectrum 3, intensity difference of the spectrum 1 of Co^{2+} ions in the glassy phase of Co^{2+} - Yb^{3+} - Er^{3+} -doped silicate glass (CYE glass) and the spectrum 2 of Yb^{3+} - Er^{3+} -doped silicate glass (YE glass). The strongest absorption of Co^{2+} ions in glass ceramics as observed in Fig. 16.9b by the spectrum 6, intensity difference between 4 and 5 spectra, is assigned to Co^{2+} into Mg^{2+} sites of T_d symmetry in Co^{2+} -doped MgAl_2O_4 nano-crystals of the (CYE glass ceramics). As a result the absorption results are in favor of the strongest population of Co^{2+} ions rather in glass ceramics than in glass.

16.3.3.3 Discussion on the Location of Yb^{3+} Ions in Glass Ceramics

The previous analysis of TEM-EDX experiments indicates we should expect the optical transitions of the three Co^{2+} , Yb^{3+} and Er^{3+} dopants in both the SiO_2

Fig. 16.11 Concentration dependence of $x\%$ Yb^{3+} ion absorption in both glass (a) and glass ceramics (b) samples at RT. X = 2, 4, 6



glassy phase and the MgAl_2O_4 nano-crystallite phase. We will report now that spectroscopic data brings new results for these glass ceramic samples.

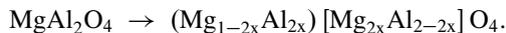
It was found out in the absorption spectra the appearance of a new absorption line between 4 K and room temperature near 970 nm, so that it was necessary to compare the absorption of different samples containing different concentrations of Yb^{3+} and Er^{3+} ions in the two hosts of glasses and glass ceramics. First, we have pointed out the double structure of the Yb^{3+} ions between 965 and 985 nm by two broad lines of practically similar intensity, so-called 0-phonon lines, with maximum at 970 and 975 nm respectively as seen in Fig. 16.11b. Previously only one peak at 977 nm was observed [19]. These two broad lines characterize the ${}^2\text{F}_{7/2} \rightarrow {}^2\text{F}_{5/2}$ transitions of Yb^{3+} ions between the lowest Stark energy level of each ${}^2\text{F}_{7/2}$ and ${}^2\text{F}_{5/2}$ manifolds rather than those of Er^{3+} ions, due to the much larger absorption coefficient of Yb^{3+} ions.

Concentration dependences of the Yb^{3+} absorption spectra of both glasses and glass ceramic samples containing the same amounts of Yb^{3+} and Er^{3+} rare earth ions are shown in Fig. 16.11a, b. Absorption spectra intensities presented for both glasses and glass ceramics are dependent on the Yb^{3+} concentration increasing. One can see the ${}^2\text{F}_{7/2} (1) \rightarrow {}^2\text{F}_{5/2} (5)$ double broad lines of Yb^{3+} 0-phonon lines with maxima at 970–975 nm. Absorption spectra of Yb^{3+} -doped glass ceramics exhibit a higher degree of structuration than that glass spectra. By comparing these absorption spectra one might assume that the line at 975 nm in glass ceramics has the same glassy origin as that in glass samples with maximum at 975.5 nm. It might be due to the presence of a double phase, like for example, both the glassy one and the nano-spinel crystalline phase with different line intensities, but this hypothesis has to be discussed as the following.

This is interesting to compare the spectra of Yb^{3+} -doped silica glass with those we obtained recently for Yb^{3+} -doped calcium alumino-silicate glasses (CAS and LSCAS) for excitation and emission spectra [30]. The spectra in these glasses are much more resolved than that of Yb^{3+} -doped silica glass, showing distinctive three ${}^2\text{F}_{7/2} \rightarrow {}^2\text{F}_{5/2}$ components of the absorption spectra and four ${}^2\text{F}_{5/2} \rightarrow {}^2\text{F}_{7/2}$ components of the emission spectra, as expected. The main reason of this difference between the two types of glasses is the presence of Ca and Al cations in the glass network of CAS and LSCAS which contribute to increase of the site symmetry inside the glassy phase. The Yb^{3+} 0-phonon line in CAS and LSCAS glasses is located at 977 nm, very close to the 975.5 nm in the silica glass of the glass ceramics, and consequently this comparison might be another proof of the assignment of the 975.5 nm peak to the silica glass phase in the glass ceramic sample.

Since the glass ceramic sample is composed of both the silicate phase and the nano-spinel crystalline phase, we also need some comparison with spectra of rare earth-doped spinel nano-crystalline phase. We have recently published the concentration dependences of the absorption spectra of Yb^{3+} -doped MgAl_2O_4 spinel nano-crystals in the range of 10–30 nm size, prepared by the sol-gel method and characterized by both structural and spectroscopic properties [31]. The first striking feature is the overlapping between the Yb^{3+} 0-phonon absorption line in the silica glass at 975.5 nm and the 0-phonon line of Yb^{3+} -doped MgAl_2O_4 spinel nano-crystals at 976 nm (Fig. 16.12).

Both of these two lines are very broad. In glasses this is due to the un-equivalent Yb^{3+} sites as usually expected in disordered amorphous materials and in MgAl_2O_4 spinel nano-crystals this is due to the following anti-site phenomenon:



Indeed, some Al^{3+} and Mg^{2+} cations are exchanged between the cation sublattices forming pairs of anti-site defects and thus a degree of inversion is created. This degree of inversion x ranges from almost 0 for the normal spinel up to 0.5 for the inverse spinel structure. Apparently, in the spinel nano-crystal phase in [19] the unresolved Yb^{3+} components indicate at large inverse spinel as a

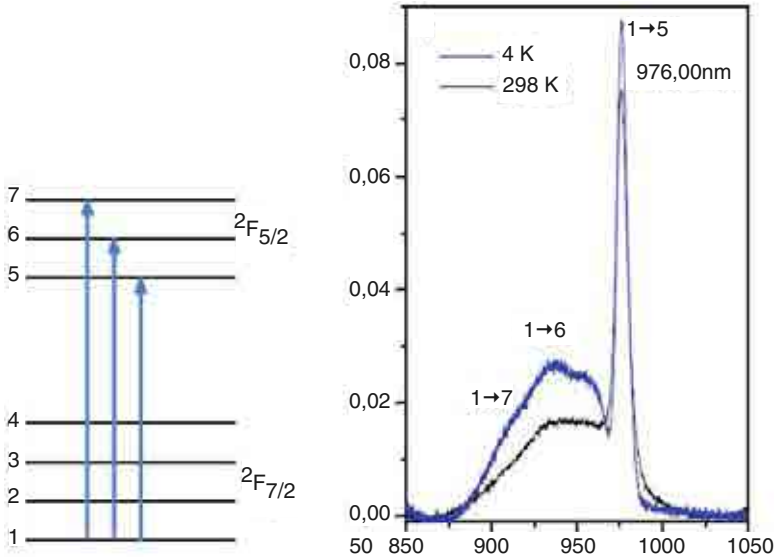


Fig. 16.12 Temperature dependence of absorption spectra of Yb^{3+} -doped MgAl_2O_4 spinel nanocrystals prepared by sol-gel method [31]

result of the multiplicity of Yb^{3+} sites observed either in octahedral or tetrahedral positions. Another effect increases the disorder by the substitution of Mg^{2+} cations. The compensation effect imposes to substitute three Mg^{2+} cations by two Yb^{3+} luminescent cations, creating one vacancy, pairs and aggregates even if the ionic radius of Yb^{3+} (85.8 pm) is much larger than those of Mg^{2+} (65 pm) and Al^{3+} (50 pm) [19]. This substitution was also proposed for the Yb^{3+} - Er^{3+} -co-doped MgAl_2O_4 phosphor powders prepared by the combustion method [32]. In addition, other perturbed Yb^{3+} ions exist due to the morphology of the surface of the grains in contrary with the regular structure of the internal grain. It means there are several reasons to increase disorder in spinel lattice and to observe large broadening of both absorption and emission spectra.

As a result, in the glass ceramic samples the line located at 975 nm can be assigned to the ${}^2\text{F}_{7/2}$ (1) \rightarrow ${}^2\text{F}_{5/2}$ (5) transition either with Yb^{3+} ions in the glassy phase or with Yb^{3+} ions in the MgAl_2O_4 inverse spinel nano-crystalline phase. There is a surprising situation, adding difficulties for the final interpretation, never reported, with two Yb^{3+} -doped phases, one with SiO_2 glass, another one with inverse MgAl_2O_4 nano-crystalline phase, which show Yb^{3+} lines in coincidence.

Consequently we can assign the line at 975 nm of the glass ceramics to both the glass and the nano-crystalline phases but the higher population detected with TEM-EDX plays in favor of the detection first of the nano-crystalline phase and like a noisy signal for the glass phase.

At last we need to find new data to interpret the absorption line at 970 nm.

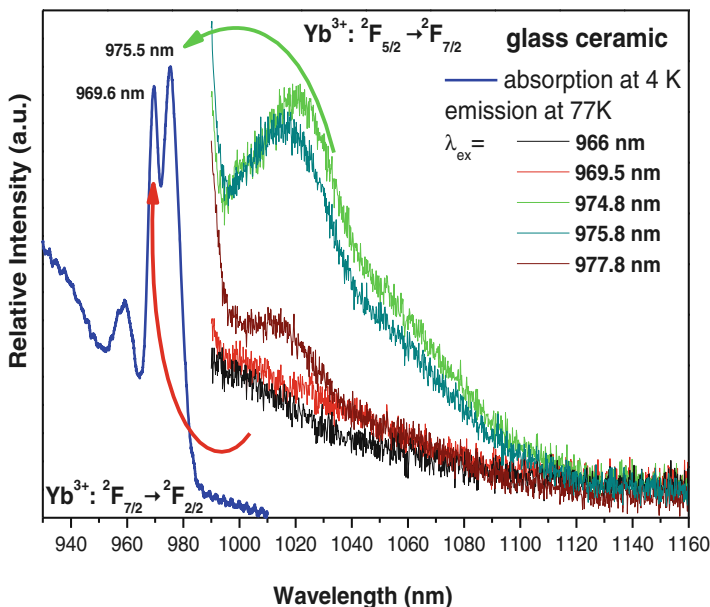


Fig. 16.13 Site selective laser excitation within the two broad ${}^2F_{7/2} \rightarrow {}^2F_{5/2}$ 0-phonon lines of Yb^{3+} ions which were detected in absorption at RT and 4 K

16.3.3.4 Site Selective Spectroscopy as a Contribution to the Assignment of the Yb^{3+} Centres

Site selective laser excitation within the range 880–950 nm of Yb^{3+} ion into the two highest excited levels of the ${}^2F_{7/2} \rightarrow {}^2F_{5/2}$ transitions of GC can be observed in Fig. 16.13 at 77 K.

The different excitations of the Ti-Sapphire laser pump are mentioned. The absorption spectrum of the sample at 4 K, almost the same as at RT, is indicated in blue as a reference. The first obvious feature is the absence of luminescence emission from Yb^{3+} ions characterized by the 0-phonon line at 970 nm. Only the Yb^{3+} 0-phonon lines around 977 nm associated to both SiO_2 glass and MgAl_2O_4 nano-crystal phases are the emitting centres shifted as expected from multi-sites in the glass ceramics. In addition we have not detected any energy transfer between the two centers responsible for these two broad absorption lines at 970 and 975 nm, respectively.

In Fig. 16.13, the site selective laser excitation at 77 K has been applied especially into the two broad ${}^2F_{7/2} (1) \rightarrow {}^2F_{5/2} (5)$ 0-phonon lines of Yb^{3+} ions which were detected in absorption with maxima at around 970 nm and 975 nm. Then, the different excitations are now in the range 966–980 nm. In red and black lines are reported the ${}^2F_{5/2} (5) \rightarrow {}^2F_{7/2} (1, 2, 3, 4)$ emission spectra under excitation at 966 nm and 969 nm, respectively into the new absorption peak present in the GC. In green,

dark blue and brown colors are reported the ${}^2F_{5/2} (5) \rightarrow {}^2F_{7/2} (1, 2, 3, 4)$ emission spectra under excitation at 974.8 nm, 975.8 nm and 977.8 nm, respectively, into the absorption peak already observed with glassy phase. We confirm only the Yb^{3+} lowest energy peak at 976 nm is giving radiative transitions and we see clearly the resolved Yb^{3+} emission spectra into excitation at 976 nm. A very weak emission is recorded under excitation at around 970 nm, due indeed to the excitation of the foot of the 976 nm absorption line since the overlapping of the two absorption peaks can't be avoided.

Consequently, the Yb^{3+} center associated with the line at 970 nm is only absorbing and not emitting. It means that the Yb^{3+} resolved emission spectra observed in Fig. 16.13 can be associated only to pumping of the broad line at around 976 nm and reflect mainly the intensity of Yb^{3+} -doped nano-spinel crystalline due to higher population of Yb^{3+} ions than in the glass.

At this point of the discussion, we interpret Yb^{3+} ions (and then associated neighbor Er^{3+} ions of similar ionic radii) in the two phases. Only Yb^{3+} -doped nano-crystalline phase is observed due to the highest population leading to higher fluorescence intensity. In the previous discussion on the emission properties we pointed out a radiation-less Yb^{3+} center associated to the 0-phonon absorption line at 970 nm only within the glass ceramic sample. Then, we think this is the result of strong perturbation acting on these centers due to the location of Yb^{3+} ions in vicinity of the surface of the nano-crystals. Such localization of this type of Yb^{3+} quencher ions on the surface close to the edges leads to stronger distortion by the crystal field than those of the regular ions inside the nano-crystal.

Another hypothesis is the presence of Yb^{3+} aggregates at the surface of nano-crystals so that migration of the energy by resonance between the 0-phonon lines at 970 nm might explain the quenching. However, TEM-EDX results did not detect any segregation of dopants at the interface of the nano-crystals and the glass and this is why we think the probability of the formation of aggregates is very weak.

16.4 Conclusion

The main goal of this work was to show how it is possible to characterize the location of Yb^{3+} and Er^{3+} rare earth ions and Co^{2+} transition metal ions by conjugating, what is rather rare, TEM-EDX and optical spectroscopy tools in a glass ceramics composed of MgAl_2O_4 spinel nano-crystals of 10–20 nm size embedded in SiO_2 glass. The application targeted is a compact self-Q-switched microchip laser for which spectroscopic properties are fulfilled. Here we have chosen this example at this School for pedagogical reasons to show the special way of assignment by applying the two independent tools of TEM-EDX and spectroscopy techniques.

The previous analysis had shown that Yb^{3+} and Er^{3+} rare earth ions seem to remain in SiO_2 glass matrix in the glass ceramics, while Co^{2+} occupy the tetrahedral sites in MgAl_2O_4 nano-crystals. The use of TEM-EDX technique led

to the result that Yb^{3+} , Er^{3+} and Co^{2+} dopants are located into the two phases but preferentially located in the spinel nano-crystals. This important result has been clearly confirmed by the elemental mapping of Yb^{3+} and Er^{3+} rare earth ions and also by the spectroscopic results of Co^{2+} ions. TEM-EDX measurements was not be accurately applied to the very low Co^{2+} concentration whereas the assignment of Yb^{3+} ion spectroscopic properties was more difficult due to the overlapping of broad ${}^2\text{F}_{7/2} (1) \rightarrow {}^2\text{F}_{5/2} (5)$ 0-phonon lines belonging to both glassy and spinel nano-crystalline phases. Yb^{3+} ions localized either in the SiO_2 glass or in the MgAl_2O_4 spinel nano-crystalline are surprisingly absorbing at almost the same wavelength, around 975 nm with the characteristic of the greatest intensity line coming from the greatest population of the spinel nano-crystalline phase. The glassy phase was not really resolved at this wavelength in the glass ceramics due to the lower intensity of the 0-phonon line. A new radiationless Yb^{3+} centre most probably localized on the strongly perturbed area of the edge of the nano-crystal surface has been pointed out by the presence of an absorption line at 970 nm of comparable intensity with that of the regular Yb^{3+} ions inside the spinel nano-crystal structure.

Triply-doped glass ceramics composed of the spinel nano-crystals imbedded in a silicate glassy phase is a good example of material for which two complementary techniques like TEM-EDX and optical spectroscopy are necessary to assign the distribution of dopants. This is the reason why it has been exposed for the School. Undoubtedly, optimization of Yb^{3+} , Er^{3+} and Co^{2+} concentrations is expected in this glass ceramics before any development.

Acknowledgements We are grateful to the CLYM (Centre Lyonnais de Microscopie, www.clym.fr) for its guidance in the Ly-EtTEM (Lyon Environmental tomographic TEM) project, which was financially supported by the CNRS, The Région Rhône-Alpes, The 'Greater Lyon' and the French Ministry of Research and Higher Education. We wish to warmly thank the Faculty of Chemistry of the University of Wrocław for the access of low temperature absorption measurements.

References

1. Maiman, T. (1960). Stimulated optical radiation in ruby. *Nature*, 187, 493.
2. Geusic, J. E., et al. (1964). Yttrium gallium and gadolinium garnets. *Applied Physics Letters*, 4(10), 182.
3. Boulon, G. (2012). 50 years of advances in solid-state laser materials. *Optical Materials*, 34(3), 499–512.
4. Pappalardo, R. G. (1987). Recent trends in laser material research. In: B. Di Bartolo, & E. Majorana (Eds.), *Spectroscopy of solid-state laser-type materials, international science series, physical sciences* (Vol. 30). New York: Plenum Press.
5. Ikesue, A., Furusato, I., & Kamata, K. (1995). Fabrication of polycrystalline, transparent YAG ceramics by a solid-state reaction method. *Journal of the American Ceramic Society*, 78, 225–228.
6. Ikesue, A., Kinoshita, T., Kamata, K., & Yoshida, K. (1995). Fabrication and optical properties of high-performance polycrystalline Nd:YAG ceramics for solid-state lasers. *Journal of the American Ceramic Society*, 78, 1033–1040.

7. Ikesue, A., Aung, Y. L., Yoda, T., Nakayama, S., & Kamimura, T. (2007). Fabrication and laser performance of polycrystal and single crystal Nd:YAG by advanced ceramic processing. *Optical Materials*, 29(10), 1289–1294.
8. Lu, J., Yagi, H., Takaichi, K., Uematsu, T., Bisson, J.-F., Feng, Y., Shirakawa, A., Ueda, K.-I., Yanagitani, T., & Kaminskii, A. A. (2004). 110 W ceramic Nd³⁺: Y₃Al₅O₁₂ laser. *Applied Physics B*, 79, 25.
9. Yagi, H., Yanagitani, T., Takaichi, K., Ueda, K.-i., & Kaminskii, A. A. (2007). Characterizations and laser performances of highly transparent Nd³⁺:Y₃Al₅O₁₂ laser ceramics. *Optical Materials*, 29(10), 1258–1262.
10. Kaminskii, A. A., Streck, W., Hreniak, D. (Eds.). (2007). *Proceedings of the 1st international laser ceramic symposium – E-MRS fall meeting 2005, 1st international laser ceramic symposium*, Warsaw, Poland, 05–06 September 2005. *Optical Materials*, 29(10), 1217–1294.
11. Sanghera, J., Kim, W., Villalobos, G., Shaw, B., Baker, C., Frantz, J., Sadowski, B., & Aggarwal, I. (2013). Ceramic laser materials: Past and present. *Optical Materials*, 35(4), 693–6991.
12. Ramirez, M. O., Wisdom, J., Li, H., Aung, Y. L., Stitt, J., Messing, G. L., Dierolf, V., Liu, Z., Ikesue, A., Byer, R. L., & Gopalan, V. (2008). Three-dimensional grain boundary spectroscopy in transparent high power ceramic laser materials. *Optics Express*, 16(9), 5965.
13. Zhao, W., Mancini, C., Amans, D., Boulon, G., Epicier, T., Min, Y., Yagi, H., Yanagitani, T., Yanagida, T., & Yoshikawa, A. (2010). Evidence of the inhomogeneous Ce³⁺ distribution across grain boundaries in transparent polycrystalline Ce³⁺-doped (Gd,Y)₃Al₅O₁₂ garnet optical ceramics. *Japanese Journal of Applied Physics*, 49, 022602. doi:10.1143/JJAP.49.022602.
14. Zhao, W., Anghel, S., Mancini, C., Amans, D., Boulon, G., Epicier, T., Shi, Y., Feng, X. Q., Pan, Y. B., Chani, V., & Yoshikawa, A. (2011). Ce³⁺ dopant segregation in Y₃Al₅O₁₂ optical ceramics. *Optical Materials*, 33, 684–687.
15. Esposito, L., Hostasa, J., Piancastelli, A., Toci G., Pirri, A., Vannini, M., Epicier, T., Malchère, A., Alombert-Goget, G., & Boulon, G. (2014). Fabrication and laser performance of multilayered YAG-Yb³⁺:YAG ceramics. *Journal of Materials Chemistry C*, 2, 10138–10148.
16. Epicier, T., Boulon, G., Zhao, W., Guzik, M., Jiang, B., Ikesue, A., & Esposito, L. (2012). Spatial distribution of the Yb³⁺ rare earth ions in Y₃Al₅O₁₂ and Y₂O₃ optical ceramics as analyzed by TEM. *Journal of Materials Chemistry*, 22, 18221–18229.
17. Chani, V. I., Boulon, G., Zhao, W., Yanagida, T., & Yoshikawa, A. (2010). Correlation between segregation of rare earth dopants in melt crystal growth and ceramic processing for optical applications. *Japanese Journal of Applied Physics*, 49, 0756011–0756016.
18. Duan, X. L., Yuan, D. R., Cheng, X. F., Wang, Z. M., Sun, Z. H., Luan, C. N., Xu, D., & Lv, M. K. (2004). Absorption and photoluminescence characteristics of Co²⁺:MgAl₂O₄ nanocrystals embedded in sol-gel derived SiO₂-based glass. *Optical Materials*, 25(1), 65.
19. Chen, L., Yu, C., Hu, L., & Chen, W. (2012). Preparation and spectroscopic properties of nanostructured glass-ceramics containing Yb³⁺, Er³⁺ ions and Co²⁺-doped spinel nanocrystals. *Solid State Sciences*, 14, 287.
20. Kalisky, Y., Kalisky, O., & Kokta, M. R. (2008). Passively Q-switched diode-pumped Nd: YAG and Nd:YVO₄ using (Cr⁴⁺, Ca²⁺):YAG and (Cr⁴⁺, Mg²⁺):YAG saturable absorbers. *Optical Materials*, 30, 1775.
21. Kalisky, Y., Ben Amar-Baranga, A., Shimony, Y., & Kokta, M. R. (1997). Cr⁴⁺ doped garnets: Novel laser materials and non-linear saturable absorbers. *Optical Materials*, 8, 129.
22. Kalisky, Y., Ben-Amar Baranga, A., Shimony, Y., Burshtein, Z., Pollack, S. A., & Kokta, M. (1996). Cr⁴⁺ doped garnets: Their properties as non-linear absorbers. *Optical Materials*, 6, 275.
23. Kalisky, Y. (2004). Passively Q-switched diode-pumped Nd:YAG and Nd:YVO₄ using (Cr⁴⁺, Ca²⁺):YAG and (Cr⁴⁺, Mg²⁺):YAG saturable absorbers. In R. Scheps, & T. Landsberg (Eds.), *Progress in quantum electronics* (Vol. 28, p. 552).
24. Chen, W., & Boulon, G. (2003). Growth mechanism of Cr: Forsterite laser crystal with high Cr concentration. *Optical Materials*, 24(1/2), 163–168.

25. Stultz, R. D., Camargo, M. B., Birnbaum, M. (1995). Divalent uranium and cobalt saturable absorber Q-Switches at 1.5 μm , OSA, *Processing of Advanced Solid-State Lasers*, 24, 460.
26. Yumashev, K. V., Denisov, L. A., Posonov, N. N., Kuleshov, N. V., & Moncorge, R. (2002). Excited state absorption and passive Q-switch performance of Co^{2+} doped oxide crystals. *Journal of Alloys and Compounds*, 341, 366.
27. Li, P., Li, Y., Sun, Y., Hou, X., Zhang, H., & Wang, J. (2006). Passively Q-switched 1.34 μm Nd: $\text{Y}_x\text{Gd}_{1-x}\text{VO}_4$ laser with $\text{Co}^{2+}:\text{LaMgAl}_{11}\text{O}_{19}$ saturable absorber. *Optics Express*, 14(17), 7730.
28. Boulon, G., Guyot, Y., Alombert-Goget, G., Guzik, M., Epicier, T., Blanchard, N., Chen, L., Hu, L., & Chen, W. (2014). Conjugation of TEM-EDX and optical spectroscopy tools for the localization of Yb^{3+} , Er^{3+} and Co^{2+} dopants in a laser glass ceramics composed of MgAl_2O_4 spinel nano-crystals embedded in SiO_2 glass. *Journal of Materials Chemistry C*, 2, 9385–9397.
29. Boulon, G., Guyot, Y., Guzik, M., Epicier, T., Gluchowski, P., Hreniak, D., & Streck, W. (2014). Yb^{3+} ions distribution in YAG nano-ceramics analyzed by both optical and TEM-EDX techniques. *Journal of Physical Chemistry C*, 118(28), 15474–15486.
30. Guyot, Y., Steimacher, A., Belançon, M. P., Medina, A. N., Baesso, L., Lima, S., Andrade, L. H. C., Brenier, A., Jurdy, A. M., & Boulon, G. (2011). Spectroscopic properties, concentration quenching and laser investigations of Yb^{3+} -doped calcium aluminosilicate glasses. *JOSA B*, 28(10), 2510–2517.
31. Wiglusz, R. J., Boulon, G., Guyot, Y., Guzik, M., Hreniak, D., & Streck, W. (2014). Structural and spectroscopic properties of Yb^{3+} -doped MgAl_2O_4 nano-crystalline spinel. *Dalton Transactions*, 43, 7752–7759.
32. Singh, V., Kumar Rai, V., Watanabe, S., Gundu Rao, T. K., Badie, L., Ledoux-Rak, I., & Jho, Y.-D. (2012). Synthesis, Characterization, Optical absorption, luminescence and defect centres in Er and Yb co-doped MgAl_2O_4 phosphor. *Applied Physics B*, 108, 437.